Accepted manuscript at https://doi.org/10.1016/j.medengphy.2019.10.005

Computing patient-specific hemodynamics in stented femoral artery models obtained from computed tomography using a validated 3D reconstruction method

Monika Colombo[1], Marco Bologna[2], Marc Garbey[3,4], Scott Berceli[5,6], Yong He[6], Josè Felix Rodriguez Matas[1], Francesco Migliavacca[1], Claudio Chiastra[1,7]

1. Laboratory of Biological Structure Mechanics (LaBS), Department of Chemistry, Materials and Chemical Engineering "Giulio Natta", Politecnico di Milano, Milan, Italy

2. Department of Electronics, Information and Bioengineering, Politecnico di Milano, Milan, Italy

3. Houston Methodist Hospital Research Institute, Houston, TX, USA

4. University of La Rochelle, LASIE UMR CNRS, La Rochelle, France

5. Malcom Randall VAMC, Gainesville, FL, USA

6. Department of Surgery, University of Florida, Gainesville, FL, USA

7. PoliTo^{BIO}Med Lab, Department of Mechanical and Aerospace Engineering, Politecnico di Torino, Turin, Italy

Address for correspondence:

Dr. Claudio Chiastra, PhD

PoliTo^{BIO}Med Lab

Department of Mechanical and Aerospace Engineering

Politecnico di Torino

Corso Duca degli Abruzzi, 24

10129 Turin, Italy

E-mail: claudio.chiastra@polito.it

ORCID: http://orcid.org/0000-0003-2070-6142

Accepted manuscript at https://doi.org/10.1016/j.medengphy.2019.10.005

Abstract

Patients with peripheral artery disease who undergo endovascular treatment are often inflicted by in-stent restenosis. The relation between restenosis and abnormal hemodynamics may be analyzed using patient-specific computational fluid dynamics (CFD) simulations. In this work, first a three-dimensional (3D) reconstruction method, based on an in-house semi-automatic segmentation algorithm of a patient's computed tomography (CT) images with calcification and metallic artifacts, and thrombus removal is de- scribed. The reconstruction method was validated using 3D printed rigid phantoms of stented femoral arteries by comparing the reconstructed geometries with the reference computer-aided design (CAD) ge- ometries employed for 3D printing. The mean reconstruction error resulting from the validation of the re- construction method was ~6% in both stented and non-stented regions. Secondly, a patient-specific model of the stented femoral artery was created and CFD analyses were performed with emphasis on the se- lection of the boundary conditions. CFD results were compared in scenarios with and without common femoral artery bifurcation, employing flat or parabolic inlet velocity profiles. Similar helical flow struc- tures were visible in all scenarios. Negligible differences in wall shear stress (< 0.5%) were found in the stented region. In conclusion, a robust method, applicable to patient-specific cases of stented diseased femoral arteries, was developed and validated.

Keywords: peripheral artery disease; stent; computed tomography; image processing; image segmentation; computational fluid dynamics; wall shear stress; helicity; 3D printing

Accepted manuscript at https://doi.org/10.1016/j.medengphy.2019.10.005

Highlights:

1) Automatic segmentation of patient-specific femoral arteries from computed tomography

2) 3D reconstruction of patient-specific femoral artery models from computed tomography

3) In-vitro validation of the reconstruction method using stented 3D printed phantoms

4) Impact of boundary conditions on the hemodynamics of patients' femoral artery models

Abbreviations:

PAD	peripheral artery disease
SFA	superficial femoral artery
ISR	in-stent restenosis
WSS	wall shear stress
CT	computed tomography
3D	three-dimensional
CFD	computational fluid dynamics
DUS	Doppler ultrasound
HU	Hounsfield unit
ROI	region of interest
CFA	common femoral artery
STL	stereolithography
CAD	computer-aided design
TAWSS	time-averaged wall shear stress
PFA	profunda femoral artery
LNH	local normalized helicity

Accepted manuscript at https://doi.org/10.1016/j.medengphy.2019.10.005

1. Introduction

Lower limb peripheral artery disease (PAD) is a world-wide pathology affecting more than 200 million individuals [1]. This progressive arterial occlusive disease is a chronic inflammatory process and it is one of the main manifestations of atherosclerosis from the clinical viewpoint [2, 3]. Although from the latest trends 21.4% [5]. Thanks to more advanced and non-invasive diagnostic tools, treating the peripheral occlusive lesions with an endovascular approach has increased, though limited by the extension of the atherosclerotic lesion and by the pathological state of progress [6]. Focusing on superficial femoral artery (SFA), the most common and one of the longest arterial segments affected by lower limb PAD, it emerges that the use of angioplasty alone is favored for short lesions; while primary self- expanding stenting is privileged for treating medium and long lesions [7]. In the latest years, drug-coated balloon has become a mixed approach with Nitinol stents where lesions are as long as 30–40 cm. However, stenting is now considered the gold standard in treating SFA atherosclerotic lesions with an endovascular approach [8, 9]. One of the main drawbacks of stenting is in-stent restenosis (ISR) in the months after intervention [10]. This adverse event, usually diagnosed with computed tomography (CT) imaging, affects more than 115,0 0 0 patients in the USA each year, determining the failure of the endovascular treatment in 30%–40% of the cases [11]. Different systematic risk factors, mainly common to atherosclerosis, contribute to the development of ISR, such as an older age, a specific ethnicity, dyslipidemia, diabetes and a history of cardio- vascular diseases [12, 13]. In addition, a key role is played by local arterial hemodynamics [14–16]. In fact, the presence of a stent disturbs the physiological blood flow and the activity of the endothelial cells is subsequently modulated by local wall shear stress (WSS), possibly resulting in neointimal hyperplasia [16, 17]. Besides near-wall hemodynamics, recent studies have suggested that an important role is also played by the bulk

flow hemodynamics [18–22]. In particular, the presence of helical flow structures might minimize flow disturbances [22, 23] and, hence, endothelium expo- sure to low WSS, which is believed to promote atherogenesis and neointimal hyperplasia [14, 16].

Nowadays, the number of studies on the hemodynamics of femoral arteries is extremely low when compared to other vascular regions. In particular, most of these works considered non-stented femoral arteries. Only recently, a study focusing on the relationship between abnormal hemodynamics and ISR in patients treated with stents has been proposed [24]. However, the proposed vessel models were reconstructed from two angiographic views, assuming the lumen cross-sections as elliptical, and patient-specific boundary conditions were not applied. Thus, these models were characterized by limitations associated with the vessel reconstruction method from angiographic images and with the boundary conditions. In this context, the current study presents a computational framework for the hemodynamic characterization of SFA after stenting treatment, based on CT acquisition, which allows to overcome the previous limitations. In particular, the first aim of the work is the development of a three-dimensional (3D) reconstruction method from patients' CT images that enables the creation of patient-specific post-operative SFA geometries by automatically reducing stent metallic image artifacts without employing manual correction. The reconstruction method was validated using CT-based 3D printed phantoms as ground-truth. The second aim of the work is the set-up of a CFD model based on a patient-specific SFA geometry and Doppler ultrasound (DUS) images, calling attention to the impact of the boundary conditions on the fluid dynamic solution. Such a model will enable the local quantification of both near-wall and bulk flow quantities in patient-specific SFAs at different time points (i.e. after the endovascular treatment and at follow-ups).

2. Materials and methods

Fig. 1 shows a general overview of the computational framework for the hemodynamic characterization of the SFA developed here. The computational workflow starts from a patient's CT and DUS images (Fig. 1 -A). The stented femoral arteries are 3D reconstructed by means of an in-house algorithm to obtain a patient- specific geometry (Fig. 1 -B). Then, a patient-specific CFD analysis is performed by using the obtained femoral artery geometry and imposing at the inlet boundary a flow rate derived from the DUS images. Finally, near-wall and bulk flow quantities are computed (Fig. 1 -C). Details of each step of the workflow are provided in the subsequent sections.

2.1. 3D reconstruction method

The 3D reconstruction method, applied to the CT acquisition, employs a semi-automatic in-house developed segmentation algorithm made up of the following main steps (Fig. 2): pre-processing, segmentation, background and calcification correction in the non- stented lumen reconstruction, and metallic artifacts and thrombus removal in the stented lumen reconstruction. The output of the algorithm is the geometrical model of the SFA. Images elaboration was pursued using Matlab (v. 2016b, MathWorks, Natick, MA, USA).

2.1.1. Pre-processing and segmentation

During the pre-processing, CT images of interest are prepared for the subsequent segmentation. First, the intensity values are converted to Hounsfield Unit (HU) and the region of interest (ROI) is cropped to reduce the computational time.

To increase the algorithm's capability of correct segmentation, the image is resized by imposing a new fixed in-plane resolution equal to 0.25 mm, independently of the initial lower CT resolution. Lastly, the image undergoes two different enhancements. In the first enhancement, used for the segmentation step, all the intensity values are normalized to the visualization window of 40–400

HU. Then, in the error removal step, the intensity is normalized to the window of 300–600 HU. The segmentation is performed using an active contour method, which is based on a level set algorithm [25, 26]. Briefly, given an initial ROI, a function $\phi(x , y)$ is defined as follows:

$$\varphi(x, y) = dist\,(I_{BIN}(x, y)) - dist\,(1 - I_{BIN}(x, y)) + I_{BIN}(x, y) - 0 . 5 \quad (1)$$

where $I_{BIN}(x, y)$ is the binary image representing the ROI, $dist\,(I_{BIN}(x, y))$ is the distance transform computed for the binary image $I_{BIN}(x, y)$ and $dist\,(1 - I_{BIN}(x, y))$ is the distance transform computed for the negative of the ROI. The function is defined so that $\phi(x , y) < 0$ inside the ROI, $\phi(x , y) > 0$ outside the ROI, and the 0-level set of the function corresponds to the ROI contour. The active contour method based on level sets iteratively changes the function $\phi(x , y)$ and, hence, the contour of the ROI to minimize a functional (referred to as "energy") computed from the original image. The minimization of such functional (in this work, the Chan-Vese energy [27]) should lead to a contour that represents the optimal segmentation. A localized version of the active contour algorithm based on the work by Lankton et al. [26] was used. Specifically, this algorithm can segment images even in case of objects with heterogeneous intensity profiles, for which global active con- tours give poor results.

To initialize the segmentation process, the user is required to define: total occlusion presence; common femoral artery (CFA) bifurcation presence and the slice where the CFA segmentation should start; number of implanted devices in the arterial portion of interest; and ISR presence. The algorithm chooses a pivot image for segmentation, taken in the middle of the CT stack to guarantee a regime condition in lumen brightness. The user is required to define on the pivot image a circular mask as initial guess. The level set algorithm is then used to obtain the final lumen segmentation in the image. From this initially segmented and roughly corrected image, the segmentation proceeds in top-direction to reach proximal end and then from the pivot image in bottom-direction

to reach distal end. Each following slice uses the segmented region of the previous slice as new initial guess.

At the end of the sliding process along the artery, the output is a stack of segmented slices that represents a rough vessel lumen. Since the first solution still includes some errors, a segmentation correction is necessary. This automatic error removal phase depends on the following user-defined parameters:

1. a background threshold for the removal of background noise in non-stented slices (minimum intensity to consider a pixel part of the lumen and not of the background);
2. a threshold for the detection of the calcifications in non-stented slices (maximum intensity to consider a pixel part of the lumen and not of a calcification);
3. an intensity threshold used to identify the bright ring of the stent in stented slices (every pixel with intensity higher than the threshold is considered part of the stent ring);
4. an intensity threshold used to identify thrombus in the stented slices (everything below the threshold is part of the thrombus);
5. a parameter representing the number of erosion/dilatation iterations applied in the stent artifacts-removal step. Negative values refer to erosions; positive values refer to dilatation [28].

Three of the five parameters can be easily set by visual inspection (parameters 2–3: 425 HU, parameter 4: 210 HU). To set the optimal value for the background threshold (parameter 1) and the number of erosion/dilatation (parameter 5), a calibration was per- formed on the artery phantom (for further details see Section 2.3).

2.1.2. Non-stented lumen reconstruction: background and calcification removal

The first automatic correction to the segmented region is applied to remove pixels erroneously included in the non-stented lumen. The algorithm identifies and classifies the CT slices containing

the stent, by considering the intensity threshold for the stent artifact. In non-stented slices, pixels are considered part of the back- ground if their intensity is lower than the background threshold (Fig. 2, on the top left). In an analogous way, if the pixel intensity is greater than the calcification threshold, those pixels are deemed as calcium (Fig. 2, on the bottom left). Both the low and high intensity pixels are removed from the segmentation mask. Finally, the ROI is smoothed by means of morphological operators and the holes are filled.

2.1.3. Stented lumen reconstruction: metallic artifacts and thrombus removal

In considering the stented lumen, the algorithm computes slice by slice the high intensity pixels, i.e. pixels whose intensity is greater than the stent artifact threshold (Fig. 2, top right). After the computation of the skeleton of the bright annulus and its convex hull, starting from its middle line the bright annulus is progressively dilated or eroded according to the user-defined parameter. The structural element chosen is a disk of unitary dimension. Successively, if the user detects the presence of ISR in the segmentation phase, pixels with an intensity lower than the thrombus intensity are excluded from the segmented image (Fig. 2, bottom right).

2.1.4. Algorithm output

The ROI resulting from the error correction phase requires further smoothing by means of morphological operators. If the output shown in the graphical user interface is deemed acceptable, it is saved in the stereolithographic (STL) format. Indeed, the algorithm produces a patient-specific lumen model described as an unstructured triangulated raw surface. After the completion of the 3D reconstruction, the centerline of the vessel geometry is extracted using the Vascular Modelling Toolkit (VMTK) (Orobix, Bergamo, Italy, http://www.vmtk.org/) and final smoothing is performed using the Laplacian filter in MeshLab (Visual Computing Lab, ISTI-CNR, Pisa, Italy, http://www.meshlab.net/).

2.2. Patients' and experimental data

CT and DUS images of two PAD patients (56 and 64 years old) treated with stents at the Malcom Randall VA Medical Center (Gainesville, FL, USA) were considered. This study was approved by the Institutional Review Board at the University of Florida and written informed consent was obtained from the patients. The CT scanner used was Brilliance 16 (Philips, Amsterdam, Nether- lands), set with tube voltage of 120 kV (KVP), X-ray tube current of 375 mA, 512 × 512 matrix, convolution Kernel B, 2-mm slice thick- ness and 1-mm spacing between slices.

Two rigid phantoms (i.e. Phantoms A and B) were derived from the patients' CT images, acquired at 1 week post intervention (Fig. 3). The CT images were segmented using the reconstruction method developed in our study and the patient-specific geometries were designed using the computer aided design (CAD) soft- ware Rhinoceros (v.5, Robert McNeel & Associates, Seattle, WA, USA). The phantoms' CAD geometries were obtained by means of a Boolean subtraction between a rectangular element and the arterial lumen surface. Finally, the phantoms were 3D printed at the University of Florida by means of the PolyJet technology, adopting a rigid translucent VeroPlus-like material and a resolution of 0.014 mm.

The rigid phantoms underwent two experimental phases. Briefly, the first one aimed at finding the correct intensity of the filling volume, i.e. the right concentration of contrast agent (Omnipaque (Iohexol) 300, GE Healthcare, Chicago, IL, USA). To replicate the patient's blood CT intensity (~200 HU), the proper volumetric concentration of the contrast agent was found to be 3.5% in 0.9% saline. The second experiment was carried out to replicate the patient's CT acquisition. First, two 6 × 80 mm Nitinol Ever-Flex TM self- expanding peripheral stent systems (EV3, Medtronic, Dublin, Ire- land), the same devices implanted in the patients, were implanted in the phantoms in 38 °C water. Once air-dried, the phantoms were filled with the 3.5% contrast agent solution and underwent a CT acquisition at the Translational Imaging Core at Houston Methodist (Houston,

TX, USA). The same scanner settings used for patients were imposed in the CT scanner Brilliance 16. Phantoms' CT images were used as input data for the 3D reconstruction method.

2.3. Calibration of the segmentation algorithm and 3D reconstruction method validation

Among the segmentation parameters, the background threshold, which depends on the concentration of contrast agent in femoral artery blood, and the number of layers for progressive dilatation, which depends on the stent material, require calibration. Moreover, the 3D reconstruction method requires validation. For this purpose, different reconstructed geometries of the phantoms were compared with the original reference CAD geometries.

Primarily, non-stented and stented lumen segmentation was calibrated adopting the 3D reconstruction of phantom A. Five different background thresholds were chosen for the non-stented lumen portion (125, 150, 175, 200, and 225 HU), while the stented portion reconstruction was neglected (number of layers, NL = 0). While the inlet and outlet cross-sections of the geometries were derived from the axial CT slices, 100 planes perpendicular to the vessel centerline and evenly spaced were created in the non-stented lumen portion using the graphical algorithm editor Grasshopper (http://www.grasshopper3d.com). For each plane, the lumen area was automatically calculated. In an analogous way, 100 corresponding planes were created in the lumen portion of the CAD reference geometry. To evaluate the best background threshold, the percentage reconstruction error for each plane was calculated as:

$$\varepsilon_{\%} = \frac{A_{rec} - A_{ref}}{A_{ref}} \qquad (2)$$

where A_{rec} is the area of the reconstructed model and A ref is the area of the CAD reference model. Then, the best background threshold was derived from the comparison between the mean percentage errors and the standard deviation.

Secondly, maintaining the best background threshold, the calibration of the stented lumen portion was performed by assigning five numbers of layers (−2, −1, 0, + 1, and + 2, where negative values indicated stent annulus erosion and expansion of the lumen, while positive values indicated the opposite). Similar to non- stented lumen calibration, for each reconstructed model and for the reference CAD model, 100 planes perpendicular to the vessel centerline were created and the stented-lumen reconstruction capability was assessed. The terminal slices, where the contrast agent was not homogenously diffused and some air bubbles were located, were excluded from the stack.

To validate the calibration results, phantom B was 3D reconstructed imposing the best segmentation parameters resulted from the previous analyses. By automatically creating planes in stented and non-stented regions, the reconstruction error was calculated and compared to that obtained for phantom A. To ensure that calibration and validation results were independent from the image dataset, a cross-validation was also performed: the best back- ground thresholds and erosion/dilatation numbers of layers were calibrated on phantom B and validated on phantom A.

2.4. CFD analyses

The aforementioned 3D reconstruction method allows the creation of a patient-specific geometry of stented femoral artery, which is suitable for CFD analyses. First, to assess how the geometry reconstruction error would affect the computed near-wall hemodynamics, a comparison was performed between the phantoms' best reconstruction obtained through the proposed 3D re-construction method and the corresponding CAD model, which was considered as ground-truth. Secondly, preliminary sensitivity analyses were carried out on the arterial geometrical model reconstructed from the patient's CT images' (the patient was used to create the phantom B). In

particular, the impact of the model boundary conditions on the hemodynamic solution was investigated.

2.4.1. Impact of reconstruction error

The CAD model of the phantoms and the best reconstruction resulting from the validation of the 3D reconstruction method were imported into ICEM CFD (v.18.1, ANSYS Inc., Canonsburg, PA, USA) and discretized using tetrahedral elements. To obtain reliable near-wall hemodynamic results, 5 layers of prismatic elements were grown with an exponential law close to the wall. The meshes were composed of ~700,000 elements with 10 quadratic and ~30 triangle elements along the inlet cross-section diameter. The element size was defined after a mesh independence study. Transient CFD analyses were performed using FLUENT (v.18.1, ANSYS Inc.). As boundary conditions, a paraboloid-shaped velocity profile at the inlet (see Section 2.4.2 for further details), zero-pressure at the outlet and no-slip condition at the lumen were prescribed. The non-Newtonian behavior of blood was modeled using the Carreau model [29]. Blood density was defined constant and equal to 1060 kg/m 3 [30]. Since the maximum Reynolds number was 1260 at the peak flow rate, the flow was assumed as laminar. The pressure-based solver with a coupled scheme for the velocity-pressure coupling was used to solve the governing equations of unsteady, incompressible fluid motion. Second order and second order upwind schemes were adopted for pressure and momentum spatial discretization, respectively. A second order implicit scheme was used for the transient formulation. The pressure and momentum under-relaxation factors were set to 0.25. The FLUENT flow Courant number was set to 50. After a sensitivity analysis, a convergence criterion of 5×10^{-5} was chosen for continuity and velocity residuals. By means of sensitivity analysis, the best temporal discretization to accomplish both reliability and cost effectiveness was found to be 100 time steps per cardiac cycle (time step size of 0.01 s) and two cardiac cycles were sufficient

for guaranteeing repeatable solution. The phantoms' CFD results were compared in terms of area-weighted average of time-averaged WSS (TAWSS) with the reconstruction geometrical error.

2.4.2. Impact of boundary conditions

The impact of the inlet boundary condition on the hemodynamic solution was evaluated by considering four different scenarios on a patient-specific model of stented femoral artery (Fig. 4):

A. SFA model without an extension imposing a flat velocity profile at the inlet and zero-pressure at the outlet ('SFA-Flat', Fig. 4 -A).
B. SFA model with a 3.5-diameter inlet extension imposing a paraboloid-shaped velocity profile at the inlet and zero- pressure at the outlet ('SFA-Par', Fig. 4 -B).
C. SFA model with upstream CFA bifurcation without an extension imposing a flat velocity profile at the inlet and the flow-split of profunda femoral artery (PFA) and SFA at the outlets ('CFA-Flat', Fig. 4 -C).
D. SFA model with upstream CFA bifurcation with an extension imposing a paraboloid-shaped velocity profile at the inlet and the flow-split at PFA and SFA at the outlets ('CFA-Par', Fig. 4 -D). This model is considered as the most complete and used as the reference when comparing CFD results.

The inlet extensions were added to 'SFA-Par' and 'CFA-Par' models to impose a paraboloid-shaped velocity profile, which needs a circular cross-section to be applied to.

In the two models containing the bifurcation, the flow split was chosen according to literature (namely 67% in SFA and 33% in PFA) [31]. The velocity waveform was patient-specific and derived from the patient's DUS image acquired at femoral level. The triphasic waveform typical of femoral arteries (Fig. 1 , DUS image) was manually extracted from the Doppler spectrum. The

sequence of peak velocities derived from DUS image was elaborated in Matlab by applying the algorithm of Ponzini et al. [32]. A Womersley velocity profile was imposed to the inlet cross-section, representing the in- let boundary condition of the CFD model. Besides the inlet and the outlet boundary conditions, the no-slip condition was applied on each wall.

Transient CFD simulations were performed using the same settings of the previous analyses. To identify the best configuration, the CFD results were examined in terms of percentage difference from the reference model, 'CFA-Par'. Similarly, to what was done to study the impact of the reconstruction error on the hemodynamics, near-wall hemodynamics was studied. The distribution of TAWSS, namely the area-weighted TAWSS and the percentage area exposed to TAWSS lower than 0.4 Pa (accepted threshold for atherogenesis [14 , 33 , 34]), was considered. The analysis was carried out in the proximal, stented and distal arterial segments. As far as bulk flow analysis is concerned, the spiral flow patterns were visualized in terms of isosurfaces of local normalized helicity (LNH) [35] , indi- cator of the distribution of the velocity field with respect to the vorticity:

$$LNH = \frac{(\nabla \times \boldsymbol{v}) \cdot \boldsymbol{v}}{|\nabla \times \boldsymbol{v}| \cdot |\boldsymbol{v}|} = \cos \alpha \qquad (3)$$

where α is the angle formed between the vorticity vector (∇ × v) and velocity vector v. Quantitatively, the bulk flow was analyzed by computing the following descriptors (Table 1): h_1 , the time-averaged value of helicity (equal to 0 in the presence of reflectional symmetry in the fluid domain); h_2 , the helicity intensity, indicator of the total amount of helical flow in the fluid domain, irrespective of direction; h_3 , non-dimensional quantity ranging between −1 and 1 indicating left-handed or right-handed helical structures, respectively; h_4 , indicator of the major rotation of helical structure (ranging between 0 and 1) [19 , 21, 22, 30] .

3. Results

3.1. 3D reconstruction method: calibration and validation results

Fig. 5 shows the cross-sectional areas along the vessel length for the 3D reconstructions obtained using different background thresholds and number of erosion/dilation layers. Specifically, the reconstructed cross-sectional area was related to the normalized vessel centerline length for the non-stented lumen in phantoms A and B (Fig. 5 -A and 5 -C) and for the stented lumen in phantoms A and B (Fig. 5 -B and 5 -D). Table 2 reports the quantitative cross-calibration results. In the parameter calibration of phantom A, the non-stented lumen was underestimated and the minimum error was acquired with threshold of 150 HU, producing a reconstruction error of −5.6% ± 4.7%. Whilst, in the stented region of phantom A, with 1-layer erosion (NL = −1) the reconstruction error was 6.5% ± 3.9%. In the validation process on phantom B, which was reconstructed with 150 HU background threshold and −1 layer, the reconstruction error was 5.9% ± 8.9% in the non-stented region and 5.4% ± 5.2% in the stented region. The results of the validation on phantom B were confirmed by the reconstruction errors evaluated in the calibration on phantom B.

3.2. CFD results: impact of the reconstruction error

Fig. 6 shows the geometric and hemodynamic comparisons between the CAD models of phantoms A and B and the corresponding best 3D reconstructions obtained using the proposed segmentation algorithm after the calibration and validation process. In particular, the cross-sectional area and the TAWSS of the two phantoms' CAD models and corresponding reconstructions were plotted with respect to the normalized vessel centerline length. Qualitatively, the curves of TAWSS of the reconstructions of the two phantoms were similar to those of the reference CAD models, both in the stented and the non-stented regions. The major discrepancies were located at the ends of

the stented regions, where the geometrical error was high. Quantitatively, the area-weighted TAWSS percentage difference between the CAD model and the best reconstruction was ~1.5% and ~2.9% for phantoms A and B, respectively.

3.3. CFD results: impact of boundary conditions

Fig. 4 shows the velocity profiles at the cross-sections corresponding to the SFA inlet for each patient-specific stented SFA model with different boundary conditions. In the bifurcated models, the velocity profiles at the SFA inlet cross-section were neither flat nor paraboloid shaped, and the 'CFA-Flat' and 'CFA-Par' models had similar velocity profiles in SFA.

The distributions of TAWSS were similar in all cases (Fig. 7). Slight differences were noticeable at the proximal vessel region close to the SFA inlet and at the stent site. Examining the quantitative results of area-weighted average TAWSS (Table 3 -A), the highest percentage differences between the different models were present at proximal SFA, with values higher than 2% with respect to the model 'CFA-Par'. Small percentage differences (< 0.5%) were observed at the stented region. Comparing the percentage area with TAWSS lower than 0.4 Pa (Table 3 -B), the lowest difference (< 0.1%) was found between the bifurcated models at the stent site. However, the difference was ~6% in the proximal segment.

Regarding bulk flow (Fig. 8 and Supplemental Figures S1 and S2), it is worth noting that, although the general topology of helical structures was maintained, small differences between the flat-profile and the paraboloid-shaped profile scenarios (i.e. 'CFA- Flat' and 'CFA-Par') were visible. By examining the helicity indexes (Table 4), it was evinced that the orientation of helical flow structures was mainly right-handed in all models but 'SFA-Flat'. The time-averaged value of helicity h_1 was close to 0 in SFA models and it increased in the bifurcated models. In observing the major rotational direction h_4, when the bifurcation is included, the helical flow structures were more relevant with a more evident major rotation.

4. Discussion

Abnormal hemodynamics has been deemed a contributing factor for restenosis in different cardiovascular regions [36–38]. Until now, few CFD studies have focused on diseased femoral arterial segments [24, 39–41]. In most of those studies [39–41], idealized geometrical models were employed to investigate hemodynamic descriptors such as WSS, oscillatory shear index and particle residence time, or the effect of the lesion location along the femoral artery. Realistic vessel curvature and tortuosity, factors particularly present in the SFA [42], were not modeled. The stent presence was taken into account only by Gogineni et al. [40] , employing an ide- alized model of the bifurcated femoral artery, and by Gökgöl et al. [24] , where non-bifurcated image-based models were considered. In particular, this last work focused on the link between hemo- dynamics and ISR, but it was limited by the image quality de- riving from 2D angiography and by the boundary conditions not specific to the patients. Moreover, a comparison between the lo- cal WSS field immediately after stent implantation and the local lumen changes at follow-up could not be conducted. In the cur- rent study, a methodological framework to locally investigate the effects of hemodynamics on restenosis in patient-specific stented SFA models is presented.

The accurate calculation of WSS is strictly dependent on the detail level of the vessel geometry, which is derived from clinical images [43]. Two main factors influence the quality of the reconstructed geometry, namely the imaging technique, with its specific resolution and limitations (e.g. presence of metallic artifacts in the vessel images in case of deployed stent), and the 3D re- construction method. Referring to peripheral limbs, CT imaging has become a preferential technique in diagnosing disease and monitoring treatment outcomes [44]. Unfortunately, despite the relevant improvements [45], the derived patient-specific information results in limited resolution and the reconstruction errors, if not corrected, may highly affect the CFD results, in

particular along the stented regions. Moreover, to avoid operator-dependence in the correction phase, a semi-automatic correction of the reconstruction errors could reduce the processing time and the variability of the reconstructed models [46] . In this work, a semi-automatic method for the 3D reconstruction of stented SFA starting from CT images was developed. Compared to other image processing methods, such as region growing, the presented algorithm allowed a better reconstruction of the stented portion of the lumen, i.e. the image portion most affected by stent artifacts. In particular, by employing the present algorithm, the stented lumen was not under-estimated, especially in the area of the brilliant annulus, which is wrongly reconstructed if employing intensity-based methods with- out any manual operation. The reconstruction capability of this method was verified using rigid 3D printed phantoms for calibration and validation purposes. Generally, most of the validations are performed comparing the automatic segmentation against the manual one. Here, the validation was based on in-vitro observations. A similar approach was followed in a previous study [47], which was, however, focused on a 3D reconstruction method of stented coronary arteries from optical coherence tomography, an imaging technique presenting a resolution much higher than CT.

The comparison between the phantom lumens reconstructed with the proposed method and the reference CAD geometries resulted in a small mean percentage reconstruction error (~6%) both in the stented and non-stented vessel regions. The reconstructions were obtained semi-automatically and required approximatively 10 min on a desktop computer (i7-950 @3.07 GHz, 16 GB RAM). Although a good reconstruction of the non-stented regions might be obtained also with commercial software based on image intensity thresholding for the segmentation process, the stented region would require manual operations to reduce the metallic artifacts usually without the possibility of imposing a new resolution to the images for erosion/dilatation operations.

The impact of the reconstruction error on the computed hemodynamics was analyzed by comparing the TAWSS results of the best 3D reconstructions of the two phantoms with respect to those of the corresponding CAD models, which represent the ground-truth. Local discrepancies were found along the vessel length, in particular at the stent ends. However, globally the TAWSS percent- age differences between the models were lower than 3%, smaller than the mean reconstruction error.

Additionally, the impact of the inlet boundary condition on the near-wall and bulk-flow hemodynamic results was investigated aiming at verifying that a patient-specific CFD model of SFA presenting the upstream CFA bifurcation provides more realistic hemodynamic information. In lights of this, we compared the hemodynamic results of less complex models (i.e. non-bifurcated models of SFA and bifurcated model with flat velocity pro- file at inlet cross-section) to the bifurcated model with inlet paraboloid-shaped velocity profile 'CFA-Par'. Differences between the investigated models in terms of TAWSS results were found at the proximal level of the SFA, highlighting that the near-wall hemodynamics was influenced, though marginally, by the type of inlet velocity profile and the insertion of the bifurcation in the CFD model. The smallest differences were observed at the ROI (i.e. stented region), proving that the more the ROI was distant from the inlet and outlet boundaries, the more the resulting quantities were comparable. The type of inlet boundary condition influenced the bulk flow hemodynamics. Although similar helical flow structures were present in all cases, the quantitative analysis showed differences between the flat-profile and the paraboloid-shaped profile scenarios, in particular in terms of helicity intensity h_2 and helical rotation balance h_4.

Finally, the developed computational framework is of general application. In fact, the 3D reconstruction method is applicable even to non-stented femoral arteries and to follow-up patients' cases presenting restenosis or not. Furthermore, it is not limited to straight leg configuration.

Although CT imaging does not particularly suffer from operator- dependence [48], the image quality and, consequently, the lumen visibility depend on the implanted stent type, determining different metallic artifacts, and on the number of CT scanner detectors [49, 50]. Hence, a limitation to our study is the necessity of the calibration of the segmentation parameters if the stent device and the CT scanner settings change. However, numerical results revealed that, after a good calibration of the segmentation parameters, the reconstruction method introduces small geometrical errors. Another limitation of the work is related to the 3D reconstruction of the detailed stent structure from CT images, which was unfeasible due to the poor resolution of this imaging technique. Besides, intravascular imaging techniques, such as optical coherence tomography, could overcome this limitation [51], but their use in the evaluation of PAD is still limited [52]. However, since the reconstructed geometry used to perform the CFD analyses is referred to 1-week follow-up, it was hypothesized that a minimal endothelialization was already present [53]. Furthermore, besides variations in cardiac frequency, the geometry and hemodynamics in SFA might be widely affected by posture and leg disposition [54]. This study was limited to a CFD model in a straight leg configuration with rigid-walls. Further fluid dynamic studies on SFA models reconstructed from CT using the proposed method might be performed taking into account the movement of the vessel.

5. Conclusions

A computational framework for the investigation of both near- wall and bulk flow hemodynamics of patient-specific stented SFA models was developed. The workflow includes a 3D

reconstruction method from CT images, which was validated using 3D printed stented SFA phantoms as ground-truth. The hemodynamic results of the best reconstructions of each phantom were compared to the corresponding CAD models, presenting smaller differences than the mean reconstruction error. Furthermore, the sensitivity analysis on the inlet boundary condition showed that the type of inlet velocity profile and the insertion of the CFA bifurcation slightly influenced the hemodynamic results. The smallest difference between the different scenarios were observed in the stented region, which was far from the boundaries.

In a wider perspective, the proposed framework can be applied to a large number of patient-specific stented SFA models to per- form reliable CFD analyses with the final aim of correlating the abnormal hemodynamics with ISR after stenting.

Declaration of Competing Interest

The authors declare no conflicts of interest.

Ethical approval

This study was approved by the Institutional Review Board at the University of Florida and conformed to the Helsinki Declaration on human research of 1975, as revised in 2000. Written informed consent was obtained from the patients. No animal studies were carried out by the authors for this article.

Acknowledgments

This work has been supported by Fondazione Cariplo, Italy (Grant number 2017-0792, TIME).

Supplementary materials

Supplementary material associated with this article can be found, in the online version, at doi: *10.1016/j.medengphy.2019.10. 005*.

References

[1] Fowkes FGR, Rudan D, Rudan I, Aboyans V, Denenberg JO, McDermott MM, et al. Comparison of global estimates of prevalence and risk factors for periph- eral artery disease in 20 0 0 and 2010: a systematic review and analysis. Lancet 2013;382:1329–40. doi: 10.1016/S0140-6736(13)61249- 0 .

[2] Ross R. Atherosclerosis-an inflammatory disease. N Engl J Med 1999;340:115– 26. doi: 10.1056/NEJM199901143400207 .

[3] Criqui MH, Aboyans V. Epidemiology of peripheral artery disease. Circ Res 2015;116:1509–26. doi: 10.1161/CIRCRESAHA.116.303849 .

[4] Cea-Soriano L, Fowkes FGR, Johansson S, Allum AM, Rodriguez LAG. Time trends in peripheral artery disease incidence, prevalence and secondary pre- ventive therapy: a cohort study in the health improvement network in the uk. BMJ Open 2018;8:e181–4. doi: 10.1136/bmjopen-2017- 018184 .

[5] Velescu A, Clara A, Peñafiel J, Grau M, Degano IR, Martí R, et al. Pe- ripheral arterial disease incidence and associated risk factors in a mediter- ranean population-based cohort. the regicor study. Eur J Vasc Endovasc Surg 2016;51:696–705. doi: 10.1016/j.ejvs.2015.12.045 .

[6] Thukkani AK, Kinlay S. Endovascular intervention for peripheral artery disease. Circ Res 2015;116:1599–613. doi: 10.1161/CIRCRESAHA.116.303503. Endovascular .

[7] Tadros RO, Vouyouka AG. A review of superficial femoral artery angioplasty and stenting. J Vasc Med Surg 2015;3:1–5. doi: 10.4172/2329-6925.10 0 0183 .

[8] Shishehbor MH. Endovascular treatment of femoropopliteal lesions: so many options, little consensus. J Am Coll Cardiol 2015;66:2339–42. doi: 10.1016/j.jacc. 2015.09.062 .

[9] Burket MW. Drug-Eluting stents are the default strategy for superficial femoral artery intervention now. Circulation 2016;133:320–9. doi: 10.1161/ CIRCULATIONAHA.115.018034 .

[10] Hamid H , Coltart J . Miracle stents–a future without restenosis. Mcgill J Med 2007;10:105–11 doi:18523610 .

[11] Tosaka A, Soga Y, Iida O, Ishihara T, Hirano K, Suzuki K, et al. Classification and clinical impact of restenosis after femoropopliteal stenting. J Am Coll Cardiol 2012;59:16–23. doi: 10.1016/j.jacc.2011.09.036 .

[12] Fowkes F, Housley E, Riemersma R, Macintyre C, Cawood E, Prescott R, et al. Smoking, lipids, glucose intolerance, and blood pressure as risk fac- tors for peripheral atherosclerosis compared with ischemic heart disease in the edinburgh artery study. Am J Epidemiol 1992;135:331–40. doi: 10.1093/ oxfordjournals.aje.a116294 .

[13] Meijer WT, Grobbee DE, Hunink MG, Hofman A, Hoes AW. Determinants of peripheral arterial disease in the elderly: the rotterdam study. Arch Intern Med 20 0 0;160:2934–8. doi: 10.1001/archinte.160.19.2934 .

[14] Malek AM, Alper SL, Izumo S. Hemodynamic shear stress and its role in atherosclerosis. J Am Med Assoc 1999;282:2035–42. doi: 10.1001/jama.282.21. 2035 .

[15] Chiu J-J, Chien S. Effects of dsisturbed flow on vascular endothelium : patho-physiological basis and clinical perspectives. Physiol Rev 2011;91:327–87. doi: 10.1152/physrev.0 0 047.20 09 .

[16] Van Der Heiden K, Gijsen FJH, Narracott A, Hsiao S, Halliday I, Gunn J, et al. The effects of stenting on shear stress: relevance to endothelial injury and re- pair. Cardiovasc Res 2013;99:269–75. doi: 10.1093/cvr/cvt090 .

[17] Liu X, Wang M, Zhang N, Fan Z, Fan Y, Deng X. Effects of endothelium, stent design and deployment on the nitric oxide transport in stented artery: a potential role in stent restenosis and thrombosis. Med Biol Eng Comput 2015;53:427–39. doi: 10.1007/s11517-015- 1250- 6 .

[18] Vorobtsova N, Chiastra C, Stremler MA, Sane DC, Migliavacca F, Vlachos P. Ef- fects of vessel tortuosity on coronary hemodynamics: an idealized and patient- specific computational study. Ann Biomed Eng 2016;44:2228–39. doi: 10.1007/ s10439-015-1492-3 .

[19] Morbiducci U, Ponzini R, Gallo D, Bignardi C, Rizzo G. Inflow boundary condi- tions for image-based computational hemodynamics: impact of idealized ver- sus measured velocity profiles in the human aorta. J Biomech 2013;46:102–9. doi: 10.1016/j.jbiomech.2012.10.012 .

[20] Gallo D, Steinman DA, Morbiducci U. Insights into the co-localization of magnitude-based versus direction-based indicators of disturbed shear at the carotid bifurcation. J Biomech 2016;49:2413–19. doi: 10.1016/j.jbiomech.2016.
02.010 .

[21] Gallo D, Steinman DA, Bijari PB, Morbiducci U. Helical flow in carotid bi- furcation as surrogate marker of exposure to disturbed shear. J Biomech 2012;45:2398–404. doi: 10.1016/j.jbiomech.2012.07.007 .

[22] De Nisco G, Kok AM, Chiastra C, Gallo D, Hoogendoorn A, Migliavacca F, et al. The atheroprotective nature of helical flow in coronary arteries. Ann Biomed Eng 2018. doi: 10.1007/s10439- 018- 02169- x .

[23] Morbiducci U, Kok AM, Kwak BR, Stone PH, Steinman DA, Wentzel JJ. Atherosclerosis at arterial bifurcations: evidence for the role of haemo- dynamics and geometry. Thromb Haemost 2016;115:484–92. doi: 10.1160/ TH15- 07- 0597 .

[24] Gökgöl C, Diehm N, Räber L, Büchler P. Prediction of restenosis based on hemodynamical markers in revascularized femoro-popliteal arteries during leg flexion. Biomech Model Mechanobiol 2019:1–11. doi: 10.1007/ s10237- 019- 01183- 9 .

[25] Drapikowski P, Domagała Z. Semi-automatic segmentation of ct/mri im- ages based on active contour method for 3D reconstruction of abdomi- nal aortic aneurysms. Image Process Commun 2014;19:13–19. doi: 10.1515/ ipc- 2015- 0 0 02 .

[26] Lankton S, Tannenbaum A. Localizing region-based active contours. IEEE Trans Image Process 2008;17:2029–39. doi: 10.1109/TIP.20 08.20 04611 .

[27] Chan TF, Vese LA. Active contours without edges. IEEE Trans Image Process 2001;10:266–77. doi: 10.1109/83.902291 .

[28] Barriga-Rivera A, Suaning GJ. Digital image processing using, 2011. Matlab; 2011. doi: 10.1109/IEMBS.2011.6091204 .

[29] Caputo M, Chiastra C, Cianciolo C, Cutrì E, Dubini G, Gunn J, et al. Simulation of oxygen transker in stented arteries and correlation with in-stent restenosis. Int J Numer Method Biomed Eng 2013;29:1373–87. doi: 10.1002/cnm .

[30] Chiastra C, Gallo D, Tasso P, Iannaccone F, Migliavacca F, Wentzel JJ, et al. Healthy and diseased coronary bifurcation geometries influence near-wall and intravascular flow: a computational exploration of the hemodynamic risk. J Biomech 2017;58:79–88. doi: 10.1016/j.jbiomech.2017.04.016 .

[31] Klein WM, Bartels LW, Bax L, Van Der GY. Magnetic resonance imaging mea- surement of blood volume flow in peripheral arteries in healthy subjects. J Vasc Surg 2003;38:1060–6. doi: 10.1016/S0741-5214(03)00706-7 .

[32] Ponzini R, Vergara C, Redaelli A, Veneziani A. Reliable CFD-based estimation of flow rate in haemodynamics measures. Ultrasound Med Biol 2006;32:1545–55. doi: 10.1016/j.ultrasmedbio.2006.05.022 .

[33] Chiastra C, Iannaccone F, Grundeken MJ, Gijsen FJH, Segers P, De Beule M, et al. Coronary fractional flow reserve measurements of a stenosed side branch: a computational study investigating the influence of the bifurcation angle. Biomed Eng Online 2016;15:1–16. doi: 10.1186/s12938-016-0211-0 .

[34] Morbiducci U, Ponzini R, Grigioni M, Redaelli A. Helical flow as fluid dynamic signature for atherogenesis risk in aortocoronary bypass. A numeric study. J Biomech 2007;40:519–34. doi: 10.1016/j.jbiomech.2006.02.017 .

[35] Vorobtsova N, Chiastra C, Stremler MA, Sane DC, Migliavacca F, Vlachos P. Ef- fects of vessel tortuosity on coronary hemodynamics: an idealized and patient- specific computational study. Ann Biomed Eng 2016;44:2228–39. doi: 10.1007/ s10439-015-1492-3 .

[36] Wentzel JJ, Gijsen FJH, Stergiopulos N, Serruys PW, Slager CJ, Krams R. Shear stress, vascular remodeling and neointimal formation. J Biomech 2003;36:681– 8. doi: 10.1016/S0 021-9290(02)0 0446-3 .

[37] Mitra AK, Agrawal DK. In stent restenosis: bane of the stent era. J Clin Pathol 20 06;59:232–9. doi: 10.1136/jcp.20 05.025742 .

[38] Morlacchi S, Keller B, Arcangeli P, Balzan M, Migliavacca F, Dubini G, et al. Hemodynamics and in-stent restenosis: micro-CT images, histology, and computer simulations. Ann Biomed Eng 2011;39:2615–26. doi: 10.1007/ s10439- 011- 0355- 9 .

[39] Javadzadegan A, Lotfi A, Simmons A, Barber T. Haemodynamic analysis of femoral artery bifurcation models under different physiological flow wave- forms. Comput Methods Biomech Biomed Eng 2016;19:1143–53. doi: 10.1080/ 10255842.2015.1113406 .

[40] Gogineni A, Ravigururajan T. Flow dynamics and wall shear stresses in a bi- furcated femoral artery. J Biomed Eng Med Devices 2017;2:1–9. doi: 10.4172/ 2475-7586.10 0 0130 .

[41] Barber T. Wall shear stress and near-wall flows in the stenosed femoral artery. Comput Methods Biomech Biomed Eng 2017;20:1048–55. doi: 10.1080/ 10255842.2017.1331342 .

[42] Wood N, Zhao S, Zambanini A. Curvature and tortuosity of the superficial femoral artery: a possible risk factor for peripheral arterial disease. J Appl Physiol 2006;101:1412–18. doi: 10.1152/japplphysiol.0 0 051.20 06 .

[43] Morris PD, Narracott A, von Tengg-Kobligk H, Silva Soto DA, Hsiao S, Lungu A, et al. Computational fluid dynamics modelling in cardiovascular medicine. Heart 2016;102:18–28. doi: 10.1136/heartjnl- 2015- 308044 .

[44] Fleischmann D, Hallett RL, Rubin GD. CT angiography of peripheral arterial dis- ease. J Vasc Interv Radiol 2006;17:3–26. doi: 10.1097/01.RVI.0000191361.02857. DE .

[45] Mahnken AH. CT imaging of coronary stents: past, present, and future. ISRN Cardiol 2012;2012:1–12. doi: 10.5402/2012/139823 .

[46] Chen W, Xu J, Chiu B, Chen W. Fast segmentation of the femoral arteries from 3D mr images: a tool for rapid assessment of peripheral arterial disease. Med Phys 2015;42:2431–48. doi: 10.1118/1.4 916 803 .

[47] Migliori S, Chiastra C, Bologna M, Montin E, Dubini G, Aurigemma C, et al. A framework for computational fluid dynamic analyses of patient-specific stented coronary arteries

from optical coherence tomography images. Med Eng Phys 2017;47:105–16. doi: 10.1016/j.medengphy.2017.06.027 .

[48] Benacerraf B. The future of ultrasound: viewing the dark side of the moon? Ultrasound Obstet Gynecol 2004;23:211–15. doi: 10.1002/uog.993 .

[49] Kaempf M, Ketelsen D, Syha R, Sixt S, Mangold S, Thomas C, et al. CT angiog- raphy of various superficial femoral artery stents: an in vitro phantom study. Eur J Radiol 2012;81:1584–8. doi: 10.1016/j.ejrad.2011.04.014 .

[50] Köhler M, Burg MC, Bunck AC, Heindel W, Seifarth H, Maintz D. Dual-Source ct angiography of peripheral arterial stents: in vitro evaluation of 22 different stent types. Radiol Res Pract 2011;2011:1–7. doi: 10.1155/2011/478175 .

[51] Chiastra C, Migliori S, Burzotta F, Dubini G, Migliavacca F. Patient-Specific modeling of stented coronary arteries reconstructed from optical coherence tomography: towards a widespread clinical use of fluid dynamics analyses. J Cardiovasc Transl Res 2017:1–17. doi: 10.1007/s12265-017- 9777-6 .

[52] Marmagkiolis K , Lendel V , Leesar MA , Feldman MD , Cilingiroglu M , K M , et al. Use of optical coherence tomography during superficial femoral artery interventions. J Invasive Cardiol 2014;26:220–3 .

[53] Bergeron P , Rudondy P , Poyen V , Pinot J , Alessandri C , Martelet J . Long-term peripheral stent evaluation using angioscopy. Int Angiol 1991;10:182–6 .

[54] Schlager O, Giurgea A, Margeta C, Seidinger D, Steiner-Boeker S, Van Der Loo B, et al. Wall shear stress in the superficial femoral artery of healthy adults and its response to postural changes and exercise. Eur J Vasc Endovasc Surg 2011;41:821–7. doi: 10.1016/j.ejvs.2011.01.006 .

Accepted manuscript at https://doi.org/10.1016/j.medengphy.2019.10.005

List of tables

Table 1. WSS and helicity-based hemodynamic descriptors

TAWSS	$\frac{1}{T}\int_0^T \lvert\mathbf{WSS}\rvert\, dt$
h_1	$\frac{1}{TV}\int_T\int_V \mathbf{v}\cdot\boldsymbol{\omega}\, dV\, dt$
h_2	$\frac{1}{TV}\int_T\int_V \lvert\mathbf{v}\cdot\boldsymbol{\omega}\rvert\, dV\, dt$
h_3	$\frac{h_1}{h_2}$ $\quad -1 \le h_3 \le 1$
h_4	$\frac{\lvert h_1\rvert}{h_2}$ $\quad 0 \le h_4 \le 1$

WSS is the WSS vector, *T* is the cardiac cycle period, ***v*** is the velocity vector, ***ω*** is the vorticity vector, *V* is the arterial volume.

Table 2. Numerical results of the calibration of the segmentation parameters for phantom A and B, in terms of correction of the background reconstruction and of the stent artifacts.

Calibration		**Phantom A**	**Phantom B**
	HU threshold	*Mean ± SD*	*Mean ± SD*
Background noise	**125**	-5.9 % ± 5.2 %	17.4 % ± 11.7 %
	150	-5.6 % ± 4.7 %	5.9 % ± 8.9 %
	175	-12.9 % ± 6.1 %	-9.6 % ± 8.9 %
	200	-29.8 % ± 7.7 %	-29.9 % ± 8.7 %
	225	-48.6 % ± 8.6%	-49.9 % ± 10.7 %
Stent artifacts	*Number of layers*		
	+2	-44.0 % ± 3.3 %	-45.8 % ± 4.1 %
	+1	-28.7 % ± 3.6 %	-29.8 % ± 4.0 %
	0	-11.4 % ± 3.6 %	-12.2 % ± 4.7 %
	-1	6.5 % ± 3.9 %	5.4 % ± 5.2 %
	-2	25.4 % ± 4.4 %	25.3 % ± 7.5 %

HU: Hounsfield Unit.

Table 3. A) Results in terms of area-weighted TAWSS. B) Relative wall area exposed to TAWSS lower than 0.4 Pa.

A	**Area-weighted TAWSS**					
	Proximal wall		**Stented wall**		**Distal wall**	
	Value [Pa]	*Percentage Difference*	*Value [Pa]*	*Percentage Difference*	*Value [Pa]*	*Percentage Difference*
SFA-Flat	1.472	7.79 %	0.804	0.49 %	1.575	4.54 %
SFA-Par	1.452	6.55 %	0.809	0.11 %	1.586	5.22 %
CFA-Flat	1.330	2.00 %	0.806	0.25 %	1.498	0.37 %
CFA-Par	1.357	/	0.808	/	1.503	/
B	**Percentage area with TAWSS ≤ 0.4 Pa**					
	Proximal wall (2986.0 mm^2)		**Stented wall (1151.2 mm^2)**		**Distal wall (710.7 mm^2)**	
	Value [%]	*Percentage Difference*	*Value [%]*	*Percentage Difference*	*Value [%]*	*Percentage Difference*
SFA-Flat	10.61 %	5.81 %	26.52 %	3.33 %	1.72 %	6.01 %
SFA-Par	11.36 %	1.23 %	26.21 %	2.18 %	1.82 %	0.55 %
CFA-Flat	11.92 %	5.80 %	25.62 %	0.09 %	1.74 %	4.92 %
CFA-Par	11.22 %	/	25.64 %	/	1.83 %	/

TAWSS: time-averaged wall shear stress; SFA: superficial femoral artery, CFA: common femoral artery; Par: parabolic inlet velocity profile; Flat: flat inlet velocity profile.

Accepted manuscript at https://doi.org/10.1016/j.medengphy.2019.10.005

Table 4. Bulk hemodynamics results in terms of helicity indexes.

	Helicity indexes			
	h_1	h_2	h_3	h_4
SFA-Flat	-0.163	6.816	-0.024	0.024
SFA-Par	0.094	8.430	0.011	0.011
CFA-Flat	0.650	8.085	0.080	0.080
CFA-Par	0.990	8.534	0.116	0.116

Par: parabolic inlet velocity profile; Flat: flat inlet velocity profile; h_1: average helicity; h_2: average helicity intensity; h_3: signed balance of counter-rotating helical flow structures; h_4: unsigned balance of counter-rotating helical flow structures.

Accepted manuscript at https://doi.org/10.1016/j.medengphy.2019.10.005

Figure captions

Figure 1. Computational framework to perform patient-specific simulations of superficial femoral artery (SFA). A) Patient's data, consisting in computed tomography (CT) and Doppler ultrasound (DUS) images. B) Patient-specific geometry of the SFA with upstream bifurcation is reconstructed using the proposed semi-automatic segmentation algorithm. C) CFD analysis of the reconstructed SFA and post-processing of the results. The output of the computational framework consists of patient-specific information in terms of both near-wall and bulk flow hemodynamics. CFA: common femoral artery; PFA: profunda femoral artery.

Figure 2. Scheme of the segmentation algorithm. After the pre-processing and the segmentation of the stack of CT images (input), correction of the reconstruction errors takes place. The correction phase is subdivided into the procedure for non-stented region (removal of the background noise and calcifications included in the reconstructed lumen) and for stented region (removal of metallic artifacts of the stent and thrombotic formations inside the lumen). For each correction step, the perimeter of the pre-correction lumen is indicated in red, while the post-correction step lumen is colored in green. The output of the algorithm is an unstructured triangulated isosurface, used for the creation of the geometrical model of the femoral artery.

Figure 3. 3D printed phantoms A and B containing self-expandable peripheral stents used for the calibration and validation of the reconstruction method (left). Computed tomography (CT) acquisition of the two stented phantoms (right).

Figure 4. Four scenarios for the analysis of the impact of the inlet boundary condition on the hemodynamic solution: A) Superficial femoral artery (SFA) model with an inlet flat velocity profile ('SFA-Flat'); B) SFA model with an inlet paraboloid-shaped velocity profile ('SFA-Par'); C) SFA model with common femoral artery (CFA) bifurcation with an inlet flat velocity profile ('CFA-Flat'); D) SFA model with CFA bifurcation with an inlet paraboloid-shaped velocity profile ('CFA-Par'). The velocity contours, obtained from CFD results, are shown for each model at several corresponding cross-sections. The vectors of velocity magnitude at SFA cross-section are shown in the boxes.

Figure 5. Results of calibration and validation of the segmentation algorithm. Areas of the lumen cross-sections with respect to the normalised vessel centerline length: A) non-stented lumen correction of phantom A; B) stented lumen correction of phantom A; C) non-stented lumen correction of phantom B; D) stented lumen correction of phantom B. The region of interest is highlighted above each plot in dark grey.

Figure 6. Comparison between the CAD model of phantoms A (left) and B (right) and the corresponding 3D reconstruction, pursued by means of the proposed segmentation algorithm, in terms of cross-sectional area (top) and time-averaged wall shear stress (bottom) with respect to the normalized vessel centerline length.

Figure 7. Computational fluid dynamics (CFD) results of the inlet boundary condition analysis in terms of contour maps of time-averaged wall shear stress (TAWSS) for all investigated scenarios. The stented region is highlighted.

Figure 8. Computational fluid dynamics (CFD) results of the inlet boundary condition analysis in terms of isosurfaces of local normalized helicity (LNH) at four time instants for the stented region of all investigated scenarios. Positive (red) and negative (blue) LNH values correspond to right-handed and left-handed rotating fluid structures along the main flow direction, respectively.

Supplementary Figure captions

Figure S1. Computational fluid dynamics (CFD) results of the inlet boundary condition analysis in terms of isosurfaces of local normalized helicity (LNH) at four time instants for the inlet region of all investigated scenarios. Positive (red) and negative (blue) LNH values correspond to right-handed and left-handed rotating fluid structures along the main flow direction, respectively.

Figure S2. Computational fluid dynamics (CFD) results of the inlet boundary condition analysis in terms of isosurfaces of local normalized helicity (LNH) at four time instants for the central region of all investigated scenarios. Positive (red) and negative (blue) LNH values correspond to right-handed and left-handed rotating fluid structures along the main flow direction, respectively.

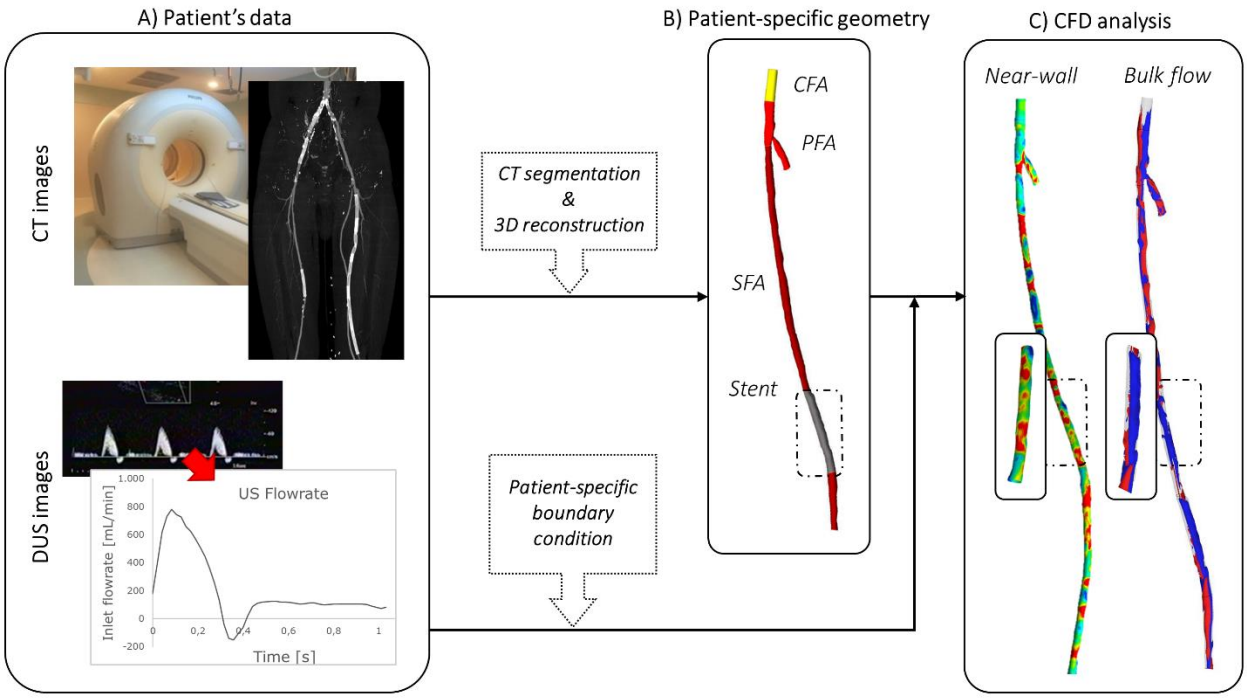

Figure 1. Computational framework to perform patient-specific simulations of superficial femoral artery (SFA). A) Patient's data, consisting in computed tomography (CT) and Doppler ultrasound (DUS) images. B) Patient-specific geometry of the SFA with upstream bifurcation is reconstructed using the proposed semi-automatic segmentation algorithm. C) CFD analysis of the reconstructed SFA and post-processing of the results. The output of the computational framework consists of patient-specific information in terms of both near-wall and bulk flow hemodynamics. CFA: common femoral artery; PFA: profunda femoral artery.

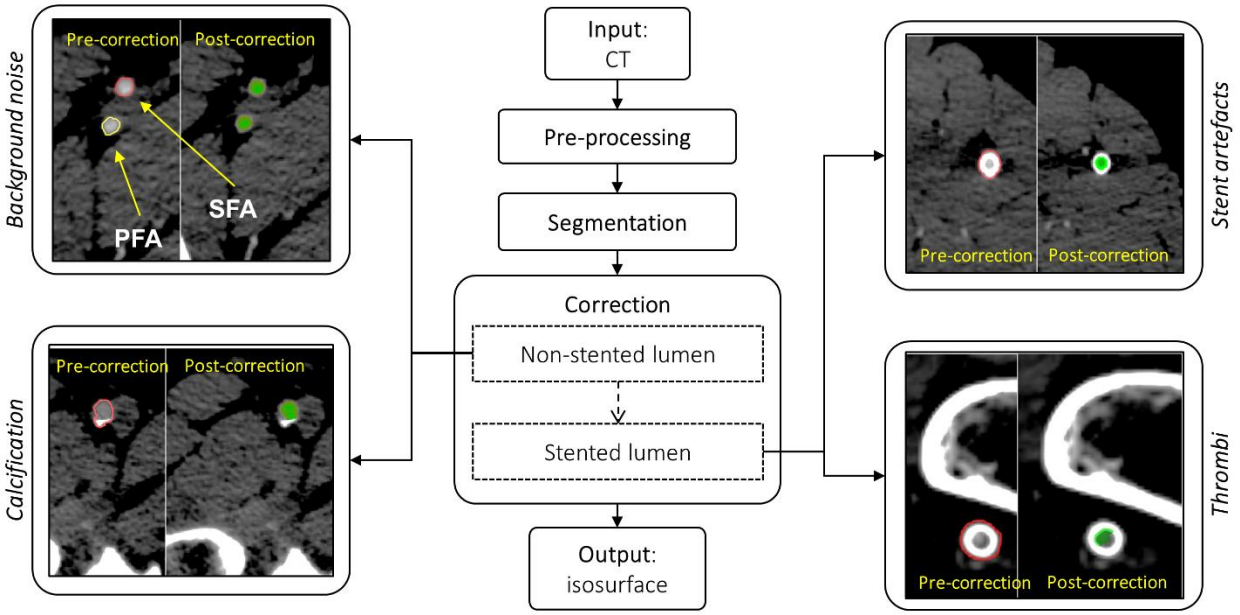

Figure 2. Scheme of the segmentation algorithm. After the pre-processing and the segmentation of the stack of CT images (input), correction of the reconstruction errors takes place. The correction phase is subdivided into the procedure for non-stented region (removal of the background noise and calcifications included in the reconstructed lumen) and for stented region (removal of metallic artifacts of the stent and thrombotic formations inside the lumen). For each correction step, the perimeter of the pre-correction lumen is indicated in red, while the post-correction step lumen is colored in green. The output of the algorithm is an unstructured triangulated isosurface, used for the creation of the geometrical model of the femoral artery.

Accepted manuscript at https://doi.org/10.1016/j.medengphy.2019.10.005

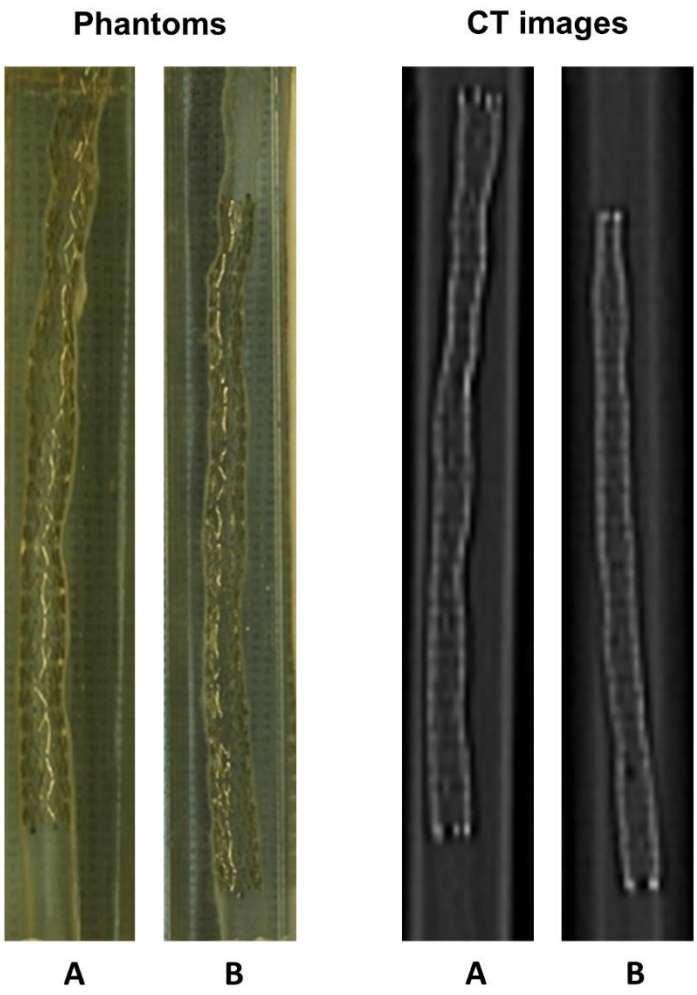

Figure 3. 3D printed phantoms A and B containing self-expandable peripheral stents used for the calibration and validation of the reconstruction method (left). Computed tomography (CT) acquisition of the two stented phantoms (right).

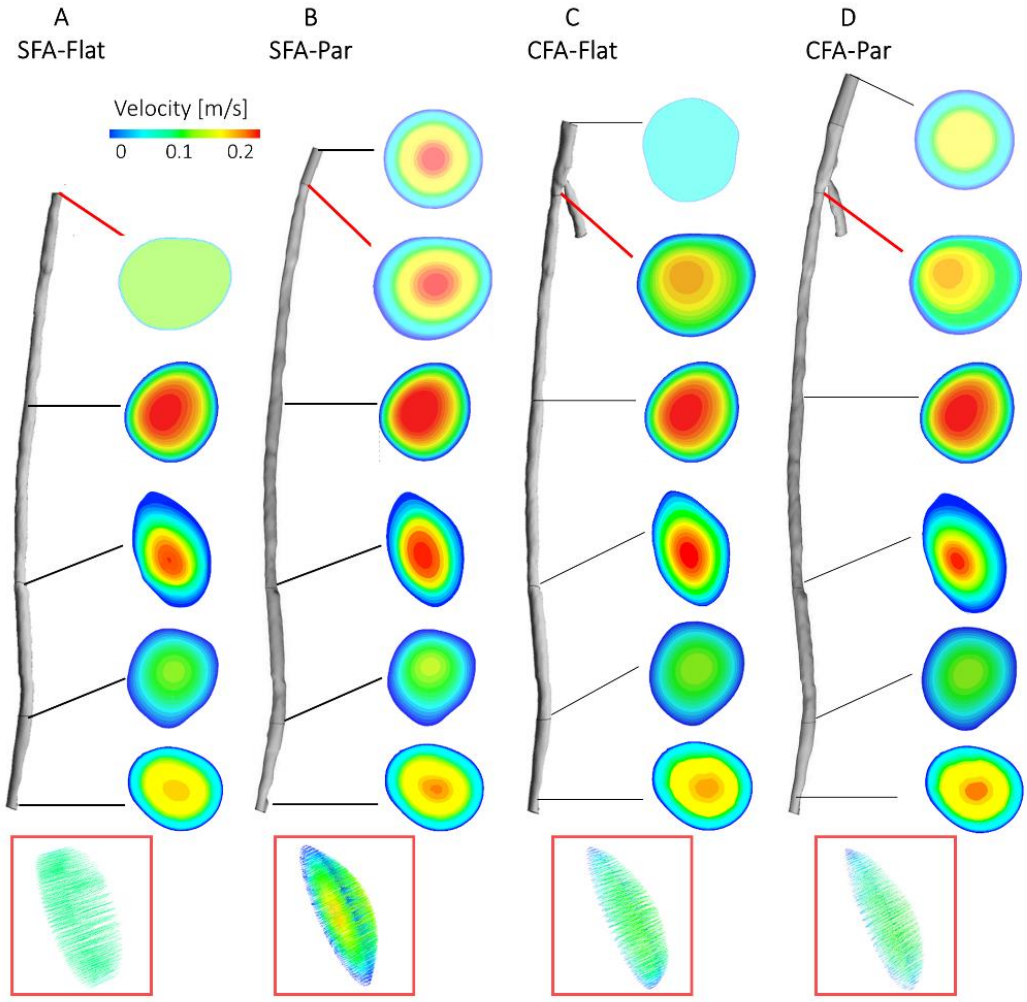

Figure 4. Four scenarios for the analysis of the impact of the inlet boundary condition on the hemodynamic solution: A) Superficial femoral artery (SFA) model with an inlet flat velocity profile ('SFA-Flat'); B) SFA model with an inlet paraboloid-shaped velocity profile ('SFA-Par'); C) SFA model with common femoral artery (CFA) bifurcation with an inlet flat velocity profile ('CFA-Flat'); D) SFA model with CFA bifurcation with an inlet paraboloid-shaped velocity profile ('CFA-Par'). The velocity contours, obtained from CFD results, are shown for each model at several corresponding cross-sections. The vectors of velocity magnitude at SFA cross-section are shown in the boxes.

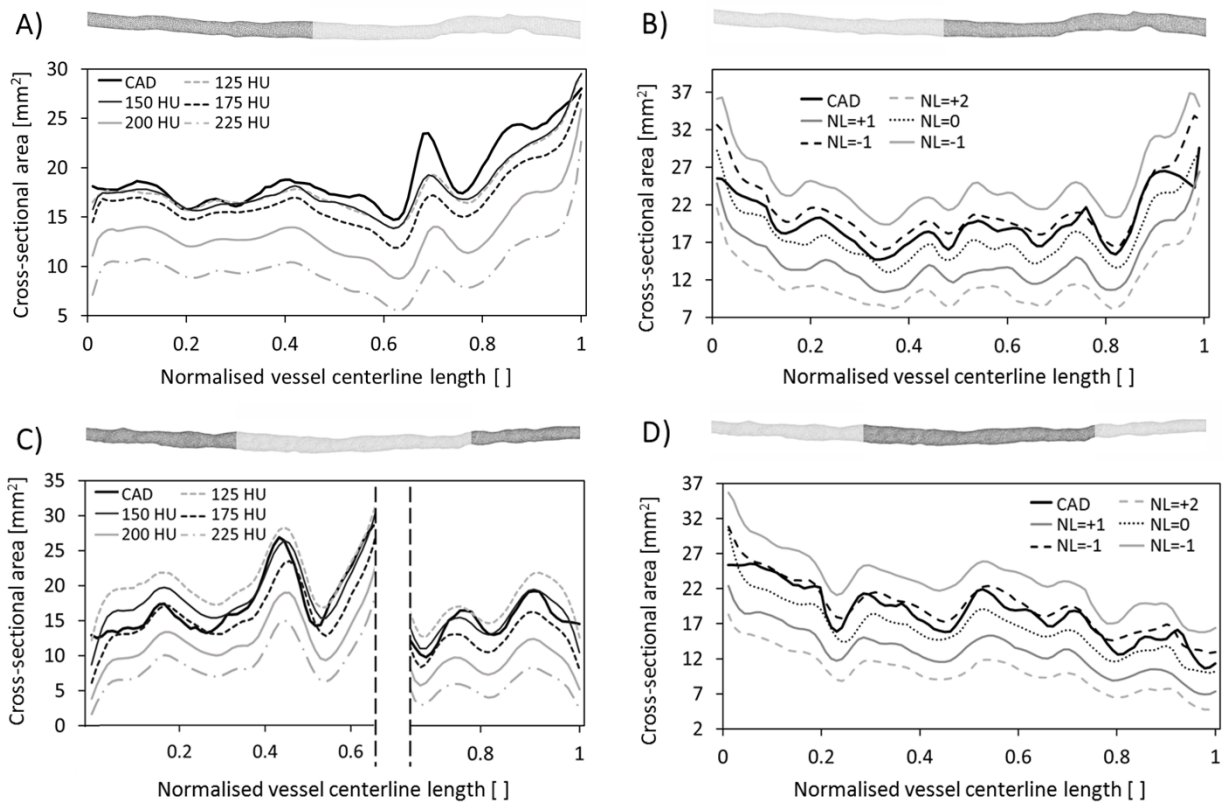

Figure 5. Results of calibration and validation of the segmentation algorithm. Areas of the lumen cross-sections with respect to the normalised vessel centerline length: A) non-stented lumen correction of phantom A; B) stented lumen correction of phantom A; C) non-stented lumen correction of phantom B; D) stented lumen correction of phantom B. The region of interest is highlighted above each plot in dark grey.

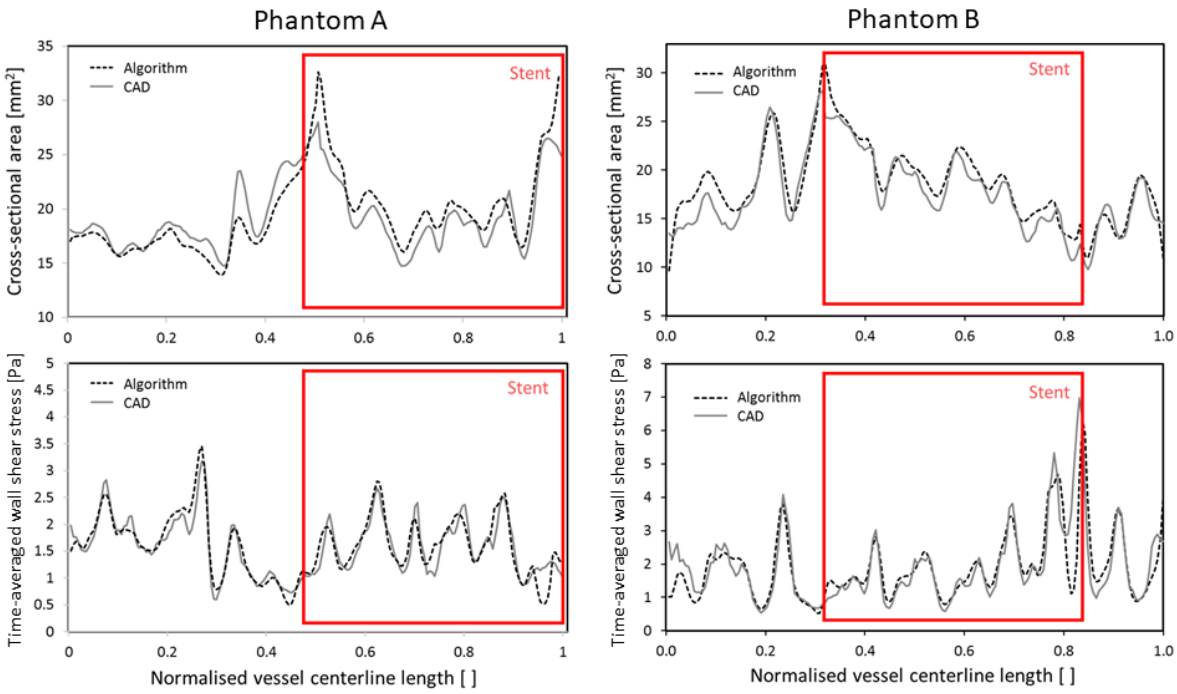

Figure 6. Comparison between the CAD model of phantoms A (left) and B (right) and the corresponding 3D reconstruction, pursued by means of the proposed segmentation algorithm, in terms of cross-sectional area (top) and time-averaged wall shear stress (bottom) with respect to the normalized vessel centerline length.

Figure 7. Computational fluid dynamics (CFD) results of the inlet boundary condition analysis in terms of contour maps of time-averaged wall shear stress (TAWSS) for all investigated scenarios. The stented region is highlighted.

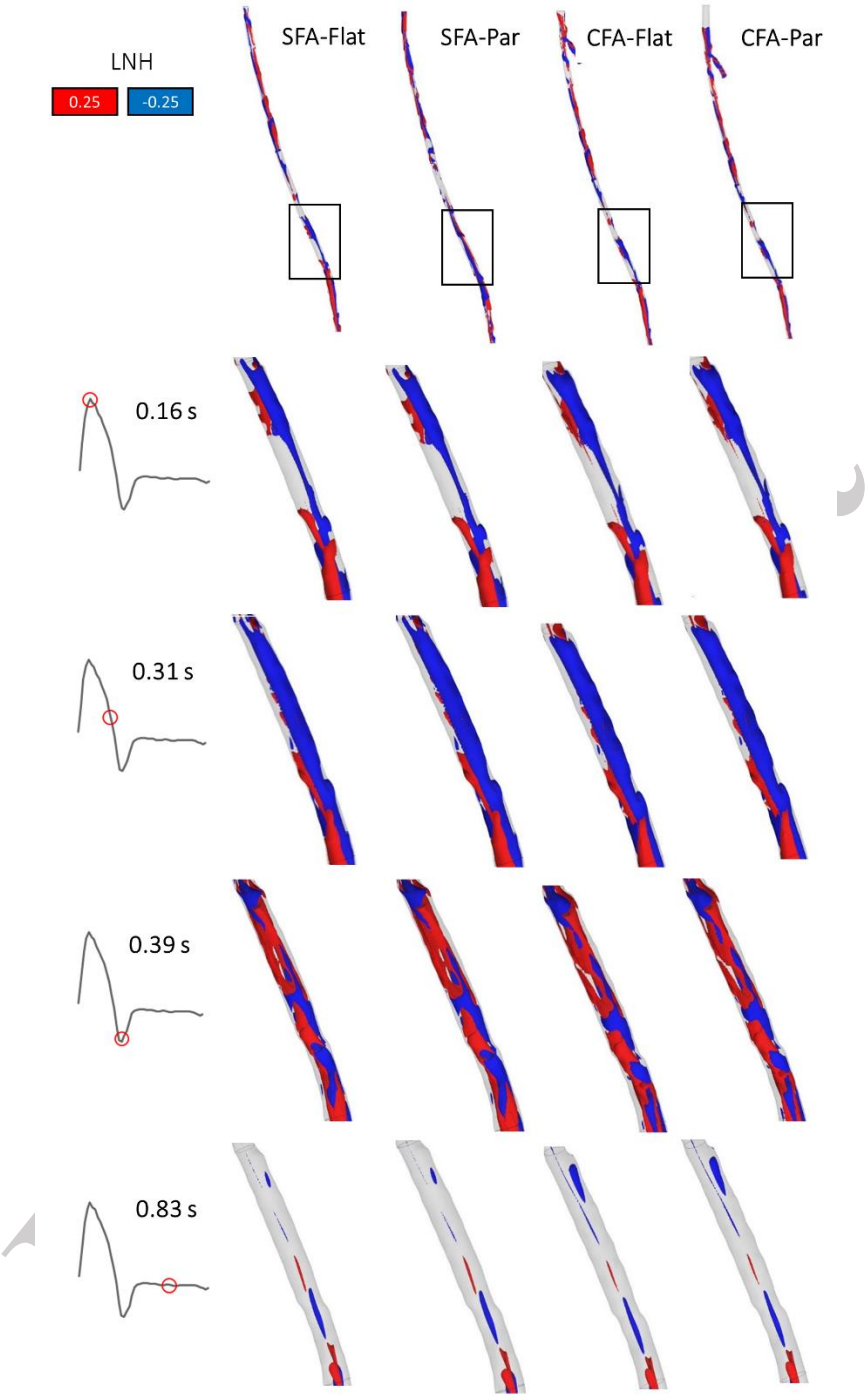

Figure 8. Computational fluid dynamics (CFD) results of the inlet boundary condition analysis in terms of isosurfaces of local normalized helicity (LNH) at four time instants for the stented region of all investigated scenarios. Positive (red) and negative (blue) LNH values correspond to right-handed and left-handed rotating fluid structures along the main flow direction, respectively.

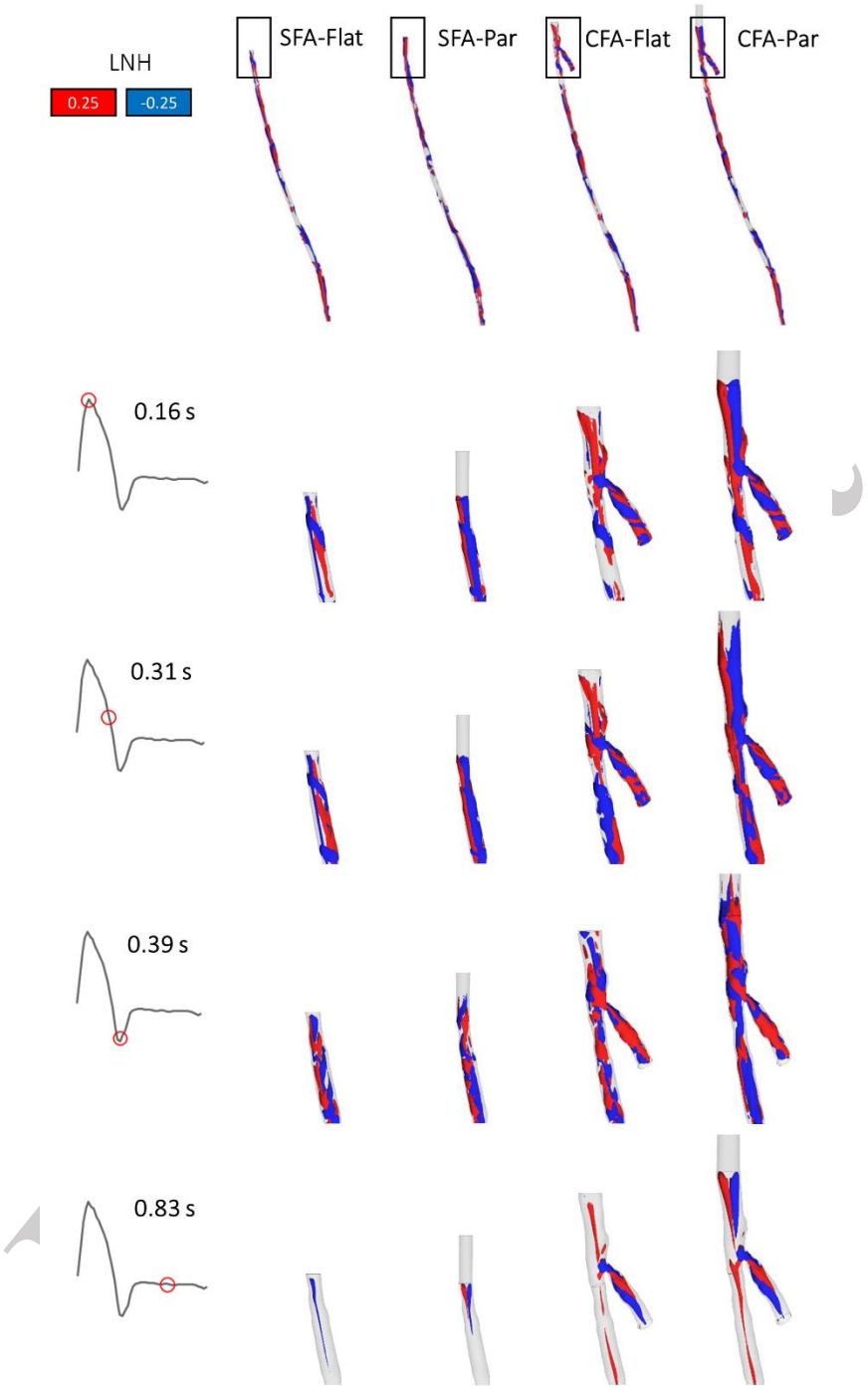

Figure S1. Computational fluid dynamics (CFD) results of the inlet boundary condition analysis in terms of isosurfaces of local normalized helicity (LNH) at four time instants for the inlet region of all investigated scenarios. Positive (red) and negative (blue) LNH values correspond to right-handed and left-handed rotating fluid structures along the main flow direction, respectively.

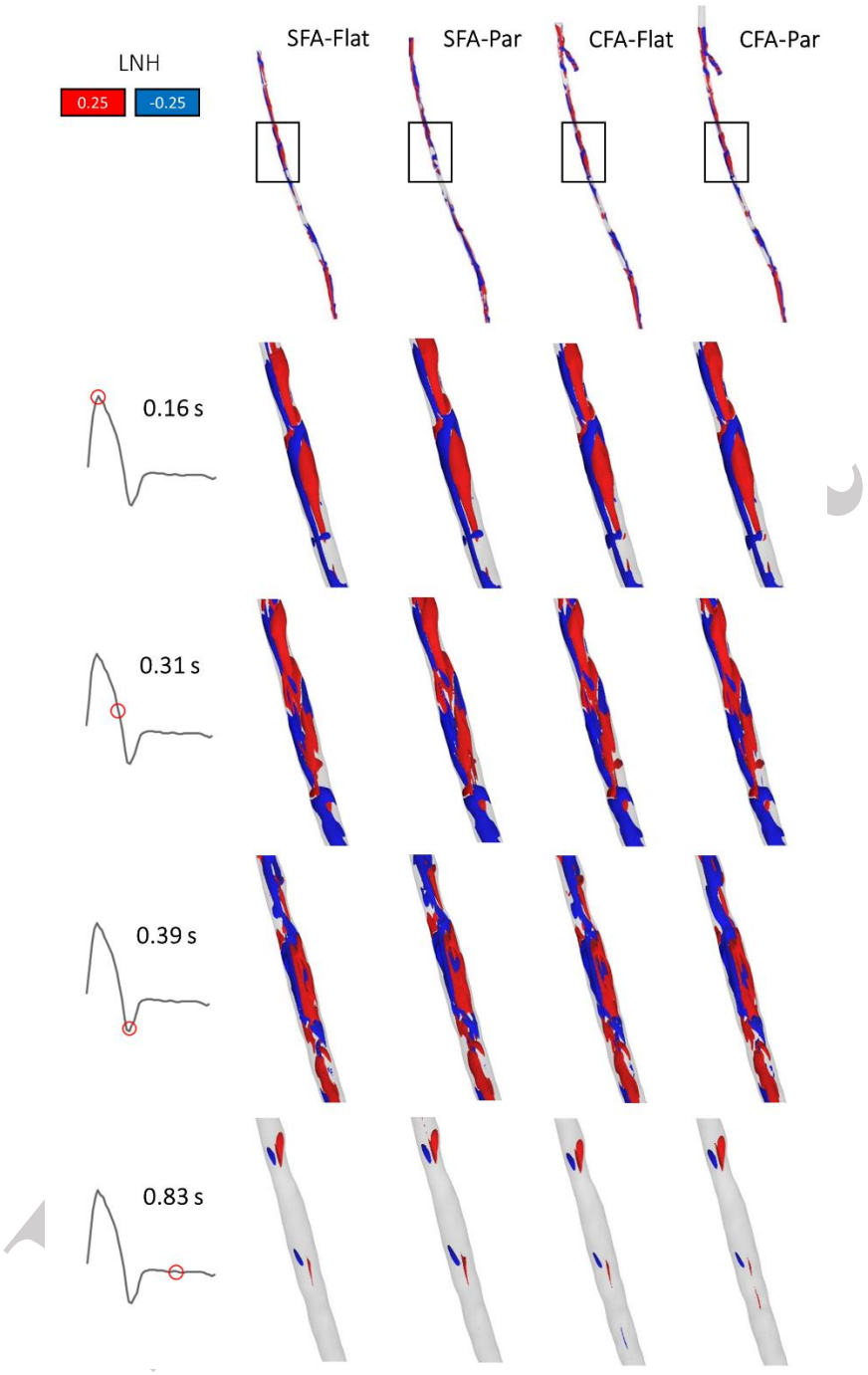

Figure S2. Computational fluid dynamics (CFD) results of the inlet boundary condition analysis in terms of isosurfaces of local normalized helicity (LN H) at four time instants for the central region of all investigated scenarios. Positive (red) and negative (blue) LNH values correspond to right-handed and left-handed rotating fluid structures along the main flow direction, respectively.